Precipitation in a mixed Al–Cu–Mg / Al–Zn–Mg alloy system

Sigurd Wenner[a], Jesper Friis[b], Calin D. Marioara[b], Randi Holmestad[a,]

[a]*Department of Physics, Norwegian University of Science and Technology (NTNU), NO-7491 Trondheim, Norway*
[b]*Materials and Chemistry, SINTEF, NO-7491 Trondheim, Norway*

Abstract

The precipitation-hardened alloy systems Al–Cu–Mg ($2xxx$) and Al–Zn–Mg ($7xxx$) were compositionally combined from a base alloy containing 2% Cu and 1% Mg, added 1–4% Zn (weight fractions). Precipitates in these alloys were studied in their peak-aged states by scanning transmission electron microscopy, focusing on qualitative and quantitative compositional measurements using energy-dispersive X-ray spectroscopy mapping. An alloy with 2.5 wt.% Zn contained both the hardening S phase from the $2xxx$ system and η-type phases from the $7xxx$ system, while alloys with 1% and 4% Zn were dominated by respectively S and η-type precipitates. The elements Mg, Cu and Zn were always present in both phases, suggesting a modification of the compositions they assume in their "native" alloy systems. Density functional theory calculations were used to investigate which atomic sites were most prone to an elemental replacement. For the η-type precipitates, calculations show that a Cu $\rightarrow$ Zn substitution leads to a decrease in formation enthalpy up to Zn/(Cu+Zn) $\approx$ 25%, which agrees well with the experimental results. For the S phase, an Al $\rightarrow$ Zn substitution was found to be the most favorable, although this increases the formation enthalpy slightly.

Keywords: Aluminium alloys, Precipitation, Transmission electron microscopy

Email address: sigurd.wenner@ntnu.no (Sigurd Wenner)

1. Introduction

The Al–Cu(–Mg) ($2xxx$) and Al–Zn–Mg(–Cu) ($7xxx$) systems encompass medium- to high-strength aluminium alloys, both applied as structural materials in a variety of fields such as aerospace, military equipment and building elements. For mechanical strength, they rely on precipitation hardening during heat treatment. The optimization of precipitation kinetics during age hardening continues to be an important area of research for both Al–Cu–Mg [1, 2, 3] and Al–Zn–Mg [4, 5, 6, 7] alloys. The equilibrium S phase in $2xxx$ alloys has a composition Al_2CuMg [8]. The orthorhombic unit cell has the lattice parameters $a = 0.400$ nm, $b = 0.923$ nm, $c = 0.714$ nm. Its coherent version adopts the Al lattice parameter 0.405 nm along its main growth direction $\langle 100 \rangle_S \,||\, \langle 100 \rangle_{Al}$. S precipitates are lath-shaped, having $\{210\}_{Al}$ habit planes (sometimes $\{410\}_{Al}$ planes), and often nucleating on defects such as dislocations and subgrain boundaries [9]. In $7xxx$ alloys, the stable precipitate phase is η, with a stoichiometric composition Zn_2Mg and hexagonal unit cell with lattice parameters $a = 0.522$ nm, $c = 0.857$ nm [10, 11]. The metastable precursor phases [12, 13, 14] all form on $\{111\}_{Al}$ planes with a disc-shaped morphology. The chemical compositions of η-type precipitates in a peak-aged 7449 alloy was studied by atom-probe tomography [15], and was estimated to (atomic fraction) 42% Zn, 7% Cu, 33% Mg and 18% Al. Atomically resolved electron energy loss spectroscopy (EELS) measurements of precipitates in the same alloy revealed that Cu atoms are replacing Zn atoms, and that this replacement has no preference for any specific Zn sites, e.g. interface sites [16].

The aim of the current paper is to investigate the compositional limits between the $2xxx$ and $7xxx$ alloy systems, whether precipitates from both systems can coexist and how additions of Cu/Zn affects the compositions of the main hardening phases in $7xxx/2xxx$ alloys, respectively. These two alloy systems were chosen for this study due to the simplicity of their precipitation sequences and hardening kinetics (compared to e.g. $6xxx$ alloys), while at the same time, their precipitates have very different crystal structures and morphology. The two classes of precipitate phases are thus expected to form individually and compete for obtaining enough solute elements to grow. The nanometer-size of the precipitated particles makes transmission electron microscopy (TEM) a suitable experimental tool, in particular since the particles may be imaged as embedded in the aluminium matrix. We study elemental substitutions in the main hardening phases by comparing energy-dispersive

X-ray spectroscopy (EDS) measurements to density functional theory (DFT) energetic stability calculations. Atomic-resolution high-angle annular dark field scanning TEM (HAADF–STEM) imaging can in principle be used to study elemental replacements at certain atomic sites due to atomic number contrast (see e.g. [17]). However, quantitative contrast measurements are infeasible for elements that are close in atomic number, such as Cu and Zn, especially when other contrast mechanisms due to e.g. strain and misorientation are likely to distort the measurements.

2. Material and methods

2.1. Experimental methods

Four alloys were investigated: a $2xxx$-like base alloy containing (weight fraction) 2.0% Cu, 1.0% Mg, 0.55% Mn and 0.20% Fe, and three alloys with the same composition added 1%, 2.5% and 4% Zn. Mn and Fe are included to create dispersoids ($Al_{20}Cu_2Mn_3$ [18, 19]) for grain refinement.

Billets were homogenized at temperatures found to be safely below all eutectic temperatures. We chose 400 °C for the 4% Zn alloy and 440 °C for all others, with the same temperatures being used for solution heat treatment (SHT). The billets were extruded to cylindrical bars with a 20 mm diameter, which were cut to 10 mm pieces for heat treatment. SHT was done in a salt furnace for 1 hour, before water quenching and direct aging at 150 °C in oil. This aging temperature is lower than what is typically used for $2xxx$ alloys, and higher than what is used for $7xxx$ alloys. During aging, Vickers hardness measurements were conducted *ex situ* with a Struers Duramin-A2500 using 5 kg load, and conductivity was measured with a Foerster Sigmatest 2.069.

TEM specimens were prepared from artificially aged material, in under-aged, peak-aged (which will be given focus) and over-aged conditions. Samples were ground/polished to roughly 100 µm thick foils, of which discs were punched out. The discs were electropolished with a Struers TenuPol-5, using a 1/3 HNO_3 and 2/3 methanol mixture, a temperature of approx. −25 °C and a voltage of 20 V. A Jeol JEM-2100F operated at 200 kV was used for HAADF–STEM imaging of precipitate microstructures. EDS maps were acquired with an Oxford Aztec EDS system on the same microscope, using a STEM probe size of about 1 nm. A double aberration-corrected (image and probe Cs) Jeol ARM-200F was briefly used for HAADF–STEM imaging at 200 kV in order to resolve precipitate crystal structures at the atomic level.

2.2. Computational methods

Upon finding that some elements from the stoichiometric composition of the precipitate phases in our alloys are substituted with other elements, we turned to quantum mechanical calculations to estimate the how the stability of the phases changes with the observed substitutions. For this purpose, density functional theory (DFT) was employed, as implemented in the Vienna ab inito simulation package (VASP) [20, 21], applying the projector-augmented wave (PAW) method [22] and Perdew–Burke–Ernzerhof exchange correlation potentials [23]. A Γ-centered k-point mesh was used in all calculations, with a maximal k-point distance of 0.25 Å^{-1} and energy cut-off above 340 eV. For structure relaxations the Methfessel–Paxton method of order one was used for partial occupancies [24] with a smearing factor of 0.2, while the tetrahedron method with Blöchl corrections were used for energy calculations.

Elemental substitutions may expand or contract the unit cell of a phase, modifying its misfit with the Al matrix. We have therefore used as supercells thin versions of the relevant phases embedded in the matrix (see Fig. 1). The two model examples are a four-layer S particle [25] and the Marioara model [13] of the GP-η_{p} precipitate [14]. The stoichiometric compositions of the models are Al_2CuMg and Zn_8Mg_3.

The formation enthalpy ΔH of the phases were estimated by subtracting the solid solution energies E_X of each of the atoms in the supercell X from the total energy of the supercell E_{Tot}:

$$\Delta H = E_{\text{Tot}} - \sum_X E_X. \tag{1}$$

We calculated E_X for the solute elements by substituting one Al atom with Mg, Cu or Zn in a supercell of 256 Al atoms in an fcc configuration:

$$E_X = E_{\text{Al}_{255}X} - \frac{255}{256} E_{\text{Al}_{256}}. \tag{2}$$

In all simulations, the supercells were first relaxed (volume, shape and atomic positions) to accommodate a full fcc lattice. No volume relaxation was carried out after elemental substitutions, with the intention of having the formation enthalpy give an indication of the coherency between the precipitate phases and the Al matrix.

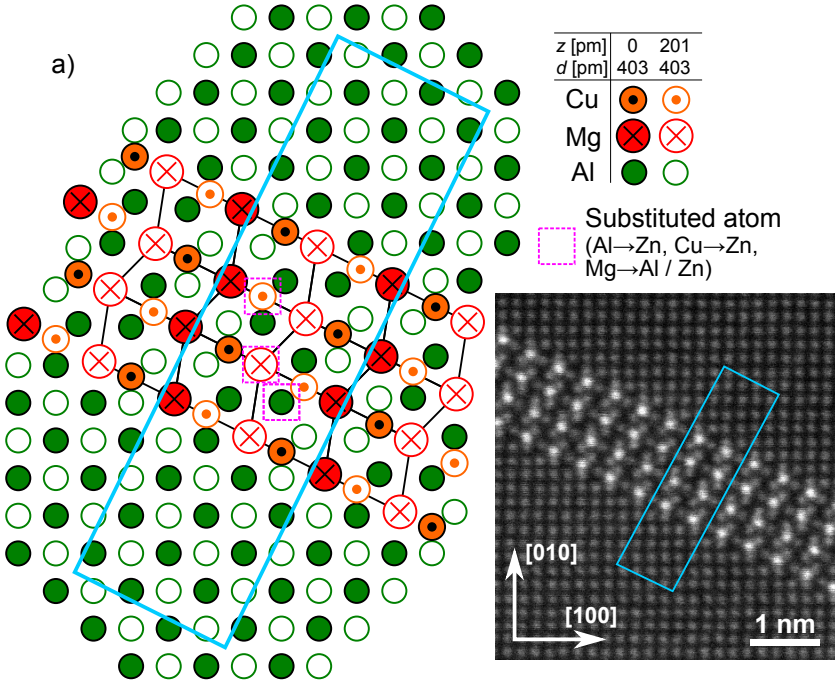

(a)

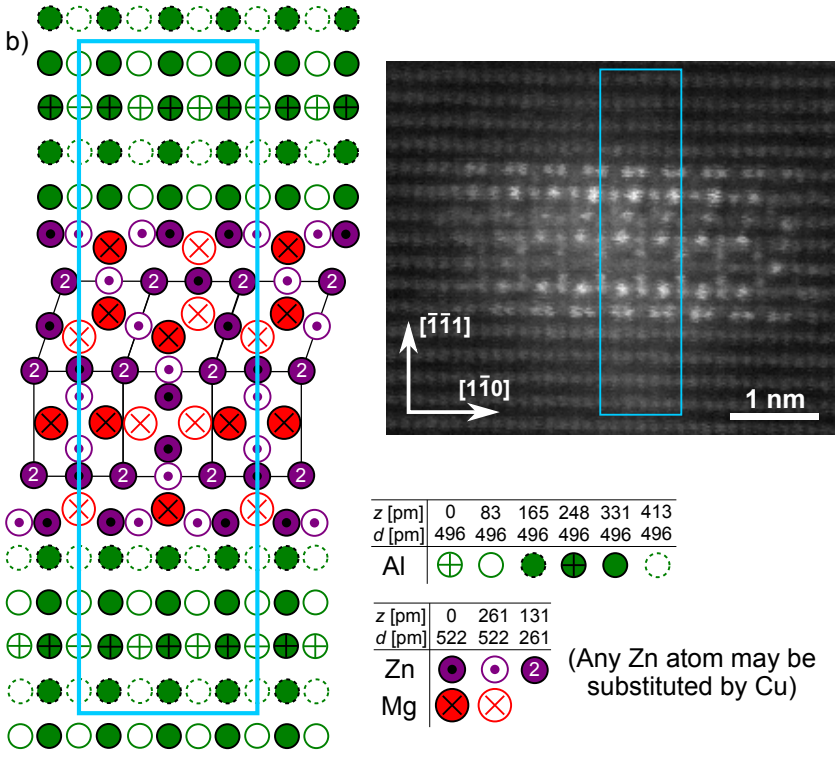

(b)

Figure 1: Supercells used in the DFT calculations of the two studied precipitate phases. The atom height normal to the paper plane is given by z, and the repeat distance by d. Experimental HAADF–STEM images are included for comparison. (a) S (Al_2CuMg), with example sites for one-atom elemental substitutions. (b) GP-η_p [14] (type 1 model from [13]). The micrograph is from [16].

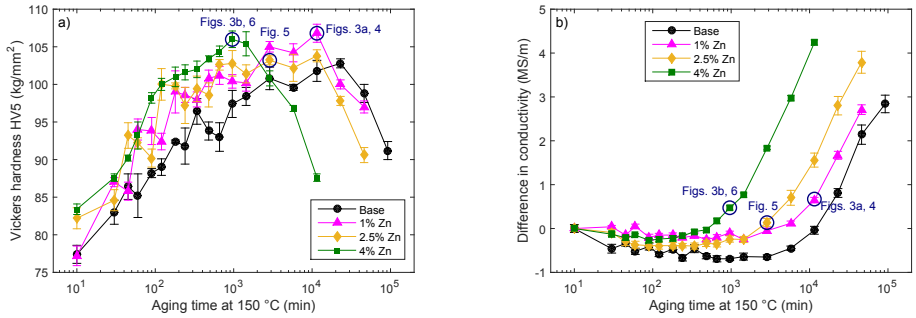

(a) (b)

Figure 2: Vickers hardness and electrical conductivity as a function of aging time at 150 °C.

3. Results

3.1. Evolution during aging

Fig. 2 shows the hardness and electrical conductivity evolution of the four alloys during isothermal aging at 150 °C. An addition of 1% Zn has a positive effect on the mechanical strength at peak age. Adding 2.5–4% Zn shifts the peak hardness state to a shorter aging time, signaling faster over-aging, while keeping the hardness value roughly constant. The same is observed among the conductivity curves, as a coarser precipitate microstructure leads to a higher electrical conductivity.

HAADF–STEM images of the precipitate microstructure at peak age are found in Fig. 3. Precipitates have a low number density compared to typical industrial alloys, and are predominately nucleated at dislocations and sub-grain boundaries. Regarding precipitate phases, the 1% Zn alloy was found to exclusively contain S and the GPB-zones of the $2xxx$ system (see e.g. [26]). The common habit planes of S were $\{210\}_{\mathrm{Al}}$ and $\{410\}_{\mathrm{Al}}$. With a Zn level of 4%, η-type plates dominate instead. Based on their thickness they can be assumed to be η_{p} [14] / type 2 precipitates [13]. Tentative heat treatments at a higher temperature (200 °C) did not affect the type of precipitates formed. As might be expected, the middle ground, represented by the 2.5% Zn alloy, is rich in both S and η-type precipitates, as seen in the next section. Rare cases of S particles were observed also in the 4% Zn alloy.

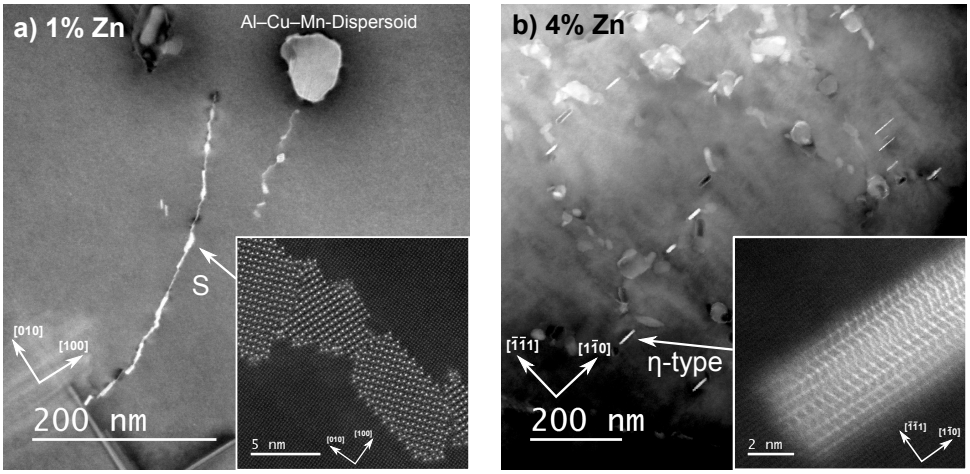

(a) (b)

Figure 3: HAADF–STEM image of the microstructures in two of the Zn-containing alloys at peak hardness. The insets show abberation-corrected images of S and η_{p} [14] / type 2 [13] precipitates in similar conditions. (a) The 1% Zn alloy aged for 8 days at 150 °C, in a $\langle 001 \rangle_{\mathrm{Al}}$ zone. (b) The 4% Zn alloy aged for 16 hours at 150 °C, in a $\langle 112 \rangle_{\mathrm{Al}}$ zone.

3.2. Compositional measurements

EDS spectrum images were acquired from precipitate-rich areas in the peak-age conditions of the three Zn-containing alloys, and elements were quantified by the Cliff-Lorimer method from the integral of their K-shell peaks. The resulting elemental maps are shown in Figs. 4–6. It is clear that the S precipitates in the 1% Zn alloy contain some Zn in their composition, and that the η-type precipitates in the 4% Zn alloy contain some Cu. The map of the 2.5% Zn alloy has a much wider field of view to highlight the presence of both S and η-type phases. The oxygen signal from Fig. 5 and 6 comes from equilibrium η particles that were oxidized during electropolishing.

The relative elemental content of the four largest (non-oxidized) precipitates in the 1% Zn and 4% Zn alloys were quantified, enabling the calculation of the fraction of substituted atoms. Aluminium is excluded from the analysis as the quantified areas may include a portion of Al matrix, giving overestimations of Al content. Thus, the following numbers are all average atomic (molar) fractions of the total Mg+Cu+Zn content. In the 1% Zn alloy, S precipitates contained 42% Mg, 52% Cu and 6% Zn. In the 4% Zn alloy, η-type precipitates contained 32% Mg, 15% Cu and 53% Zn. Many addi-

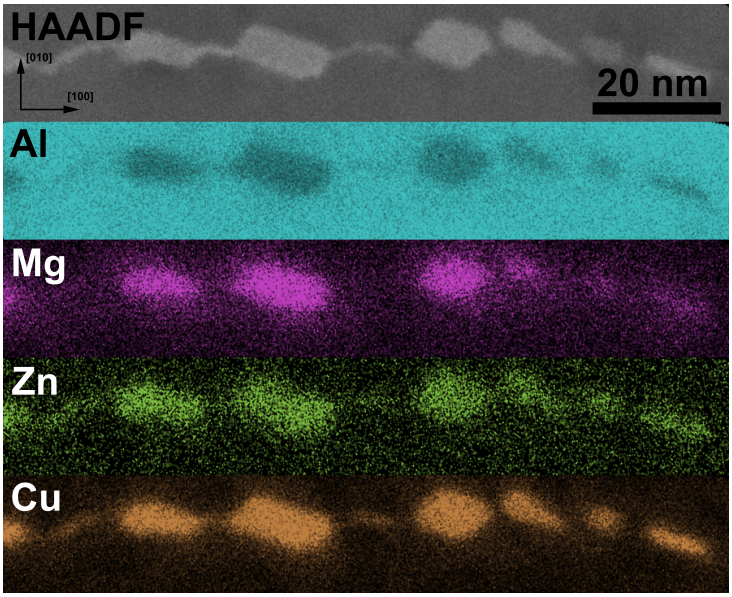

Figure 4: STEM–EDS elemental maps of S precipitates along a dislocation, in the 1% Zn alloy aged for 8 days at 150 °C. The beam direction is parallel to a $\langle 001 \rangle_{\mathrm{Al}}$ zone.

tional precipitates were studied individually by EDS measurements, and the above numbers are representative for precipitates of all sizes, interface structures/habit planes and locations within an Al grain or on a grain boundary. Fig. 7 show two example EDS spectra used for quantification.

3.3. Compositional studies by density functional theory

Judging by the elemental maps in Figs. 4 and 6, substitutions of certain elements by Zn (in S) and Cu (η-type precipitates) seem to be energetically favorable. This can be checked with calculations as described in section 2.2. For the metastable GP-η_{p} / type 1 supercell (Fig. 1(b)), Zn $\rightarrow$ Cu substitutions were found to be beneficial, and many different substitution schemes were attempted. The calculated formation enthalpies per atom are plotted in Fig. 8, together with the EDS compositional measurement from the previous section. The enthalpy is seen to decrease with initial elemental substitutions, until the Cu/(Zn+Cu) ratio is 20–30%, before increasing again. The region of lowest formation enthalpy coincide well with the experimentally measured composition. The optimal configurations are created by substituting Zn with

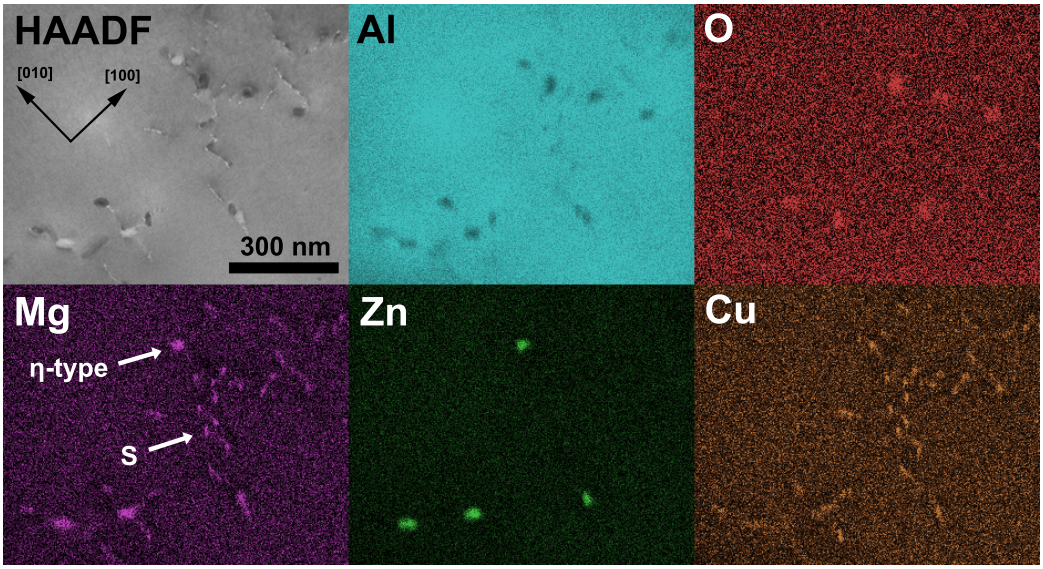

Figure 5: STEM–EDS elemental maps of a large area containing several S and η-type precipitates, in the 2.5% Zn alloy aged for 2 days at 150 °C. The beam direction is parallel to a $\langle 001 \rangle_{\mathrm{Al}}$ zone.

Cu in the following order: The "double column" sites labeled with a number 2 → the interface sites → the other interior sites (see Fig. 1(b)).

For the S supercell (Fig. 1(a)), we attempted exclusively one-atom substitutions as the measured Zn content in S precipitates is quite low. This will always give a Zn/(Mg+Cu+Zn) ratio of 6.25%, which is close to the experimentally measured value. In addition, Mg → Al substitutions were attempted to address the small Mg/Cu deficiency (as compared to the expected 1:1 ratio) measured by EDS. The resulting formation enthalpies per atom are shown in Table 1. Regardless of the substitution scheme, including Al → Mg, the formation enthalpy is higher than in the pure S case. Some additional changes to the morphology of the supercell were attempted to check if a decrease in enthalpy can be achieved, such as relaxing the supercell shape after the substitutions, and forcing strict coherency with the Al matrix in all directions. The S structure without Zn retains the lowest formation enthalpy, in contradiction to the experimental findings. The most favorable of the substitutions is found to be Al → Zn, with a +3 meV difference from pure S, irrespective of which Al site is substituted. Substitutions in the interior sites

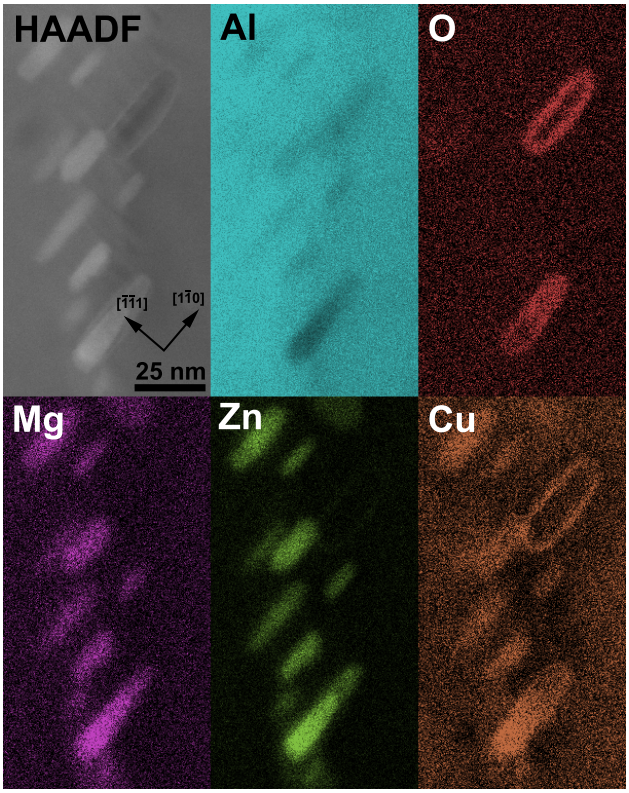

Figure 6: STEM–EDS elemental maps of η-type precipitates along a subgrain boundary, in the 4% Zn alloy aged for 16 hours at 150 °C. The beam direction is parallel to a $\langle 112 \rangle_{\mathrm{Al}}$ zone.

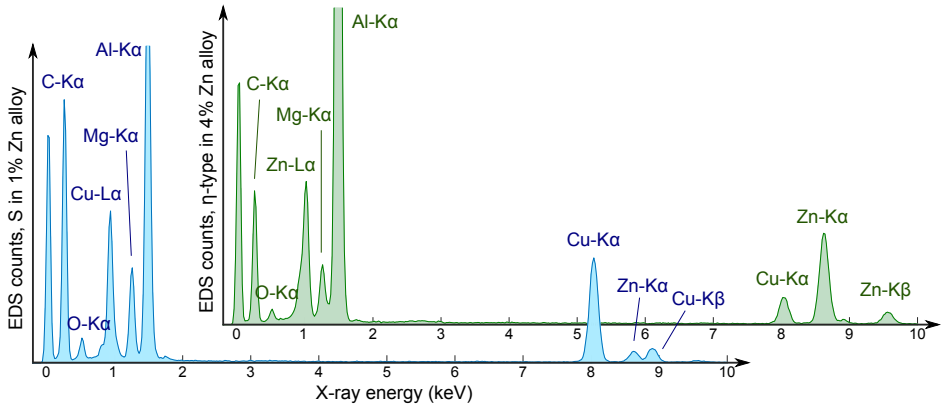

Figure 7: EDS spectra extracted from precipitates in Figs. 4 and 6, and used for quantification of Mg, Cu and Zn content.

and at the interface sites are very close in energy (≈ 1 meV) in the S case, so only the former are listed in Table 1.

Table 1: Formation enthalpy per atom of the S phase with various one-atom substitutions. The supercell with a pure structure is presented in Fig. 1(a). The reference is the solid solution enthalpy of each element.

Configuration	Enthalpy (meV)
Pure S (Al_2CuMg)	-74
Al $\rightarrow$ Zn	-71
Mg $\rightarrow$ Al	-69
Cu $\rightarrow$ Zn	-68
Mg $\rightarrow$ Zn	-64
Mg $\rightarrow$ Al and Cu $\rightarrow$ Zn	-63

4. Discussion

The rate of precipitation and coarsening in our alloys is remarkably different upon adjusting the Zn content, judging from the hardness and conductivity curves. The coarsening happens the fastest in the high Zn alloy, which is dominated by η-type precipitates. The observed lack of homogenous nucleation in the Al matrix is a common characteristic of $2xxx$ alloys [9], but

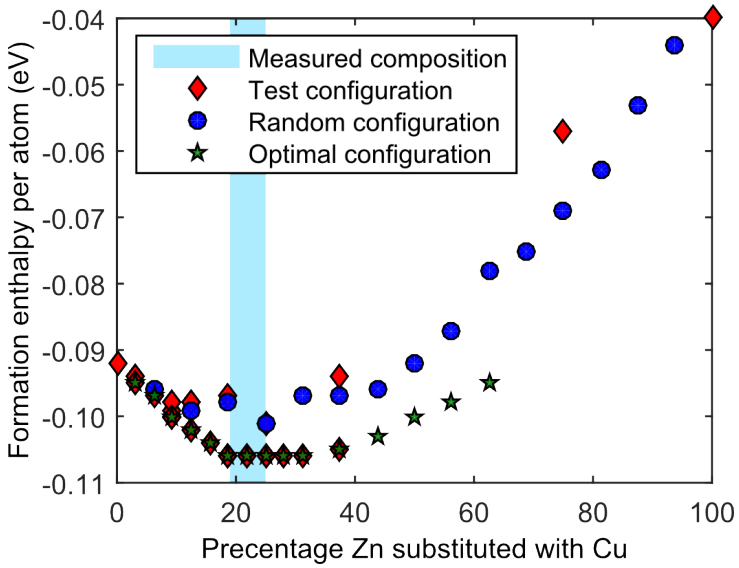

Figure 8: Formation enthalpy of the GP-η_p / type 1 supercell in Fig. 1(b), with different configurations of Cu substituted by Zn. The x-axis numbers indicate the atomic Cu/(Cu+Zn) ratio. The shaded area marks the uncertainty interval of the composition of precipitates in the 4% Zn alloy, measured by EDS.

small additions of Si would be effective for helping homogeneous nucleation (see e.g. [27]), and are therefore generally added to both $2xxx$ and $7xxx$ alloys. Some S particles were found in the 4% Zn alloy and S had a somewhat stronger presence than η-type precipitates in the 2.5% Zn alloy. This indicates that the "tipping point" between $2xxx$-like and $7xxx$-like precipitation lie at a compositional ratio Zn/Cu > 1 for the chosen heat treatment.

Precipitate compositions are not always strictly stoichiometric, but can be adaptable to the composition of the alloy. For example, the S precipitates in our alloys have an atomic ratio Mg/Cu < 1, while alloys with a higher amount of Mg can precipitate S with Mg/Cu > 1 [28]. More importantly for this study, S particles in the 1% Zn alloy contained Zn, while η-type particles in the 4% Zn alloy contained Cu. From the formation enthalpy results in Fig. 8, we see that GP-η_{p} / type 1 precipitates are stable even with a high fraction Zn replaced by Cu. The precipitates observed in the high Zn alloy were quite thick and were probably η_{p} / type 2 rather than GP-η_{p} / type 1 [13, 14], but since a Cu replacement was found to be favorable at all Zn sites, we expect the other, very similar η precursor phases to behave in the same fashion. If one keeps reducing the Zn/Cu ratio of the alloy composition, S will of course eventually nucleate and grow instead as the more favorable phase.

Table 2: Average precipitate compositions quantified by EDS, with standard deviations. The numbers are atomic fractions of the total Mg+Cu+Zn content. Compositions of model systems (S and type 1 depicted in Fig. 1) are included, with the elemental substitutions found most likely by DFT calculations. Values in parentheses are enforced.

Precipitate phase	Mg (%)	Cu (%)	Zn (%)
S in 1% Zn alloy	43 ± 6	52 ± 5	6 ± 1
S (Al_2CuMg) model, Al $\rightarrow$ Zn	47	47	(6)
S (Al_2CuMg) model, Mg $\rightarrow$ Zn	44	50	(6)
η-type in 4% Zn alloy	32 ± 1	15 ± 2	53 ± 2
type 1 (Zn_8Mg_3) model, Zn $\rightarrow$ Cu	27	(15)	58
η (Zn_2Mg) model, Zn $\rightarrow$ Cu	33	(15)	52

Zn was present in all S particles studied in the 1% Zn alloy, and the amount was irrespective of their sizes, shapes, and habit planes, e.g. many 4-layer particles growing along $\langle 112 \rangle_{\mathrm{Al}}$, as in Fig. 1(a), were checked. Nevertheless, our DFT calculations estimated that the formation enthalpy of the precipitate increases upon Cu $\rightarrow$ Zn substitutions, which means that incor-

porations of Zn should be unfavorable. The change in formation enthalpy (+3 meV) is however quite small, and could easily be reversed by taking into account effects which we have ignored in our analysis. The most apparent is that the DFT calculations are conducted at zero temperature, as opposed to 150 °C, at which precipitation occurs. Entropy would play a significant role at such an elevated temperature, favoring a more equal distribution of Zn between the matrix and the S phase. The study of the effect of temperature would require a molecular dynamics simulation, which would be too inaccurate with classical potentials, and too CPU-intensive with full electron treatment. Thus we are currently unable to confirm our suspicions about the nature of the discrepancy between experiment and calculations.

Finally we look at the average compositions found by EDS measurements and compare them to stoichiometric configurations with optimal elemental substitutions. Table 2 shows these results, fixing the substituted amounts of (Al,Mg) → Zn in S and Zn → Cu in η-type phases. The correspondence between the models and EDS data is within the experimental standard deviations when we assume initial compositions of Al_2CuMg and Zn_2Mg, respectively. For the S phase, both Al → Zn and Mg → Zn substitutions give an acceptable match, but the former is more likely based on the formation enthalpy found by DFT.

5. Conclusions

Al alloys with 2.0% Cu, 1.0% Mg, 0.55% Mn, 0.20% Fe and a variable amount of Zn was studied by STEM/EDS, and DFT simulations of S and η-type precipitate phases were performed with elemental substitutions from the generally accepted stoichiometric compositions. The microstructures of the peak hardness conditions were dominated by coherent S and η-type precipitates in the 1% Zn and 4% Zn alloys, respectively, with the 2.5% Zn alloy containing both phases. With the alloy compositions in this study, η-type phases over-age/coarsen faster than S at 150 °C, as seen in the accelerated hardness curves for the high-Zn alloys. The two classes of phases have a similar hardening potential, and the presence of both phases do not affect the strength appreciably.

EDS maps reveal that both phases contain all elements Mg, Cu and Zn. Aided by DFT calculations, we find that the most favorable replacements are Al → Zn in the S phase and Zn → Cu in η-type phases. In the latter case, the atomic ratio is measured to Cu/(Cu+Zn) ≈ 22%, which corresponds well

with the minimum in formation enthalpy from the DFT calculations. The direct experimental verification of the specific elemental replacement sites found by DFT is a very difficult task. Contrast in HAADF–STEM is too weak and unpredictable to give a final verification, and electron energy loss spectroscopy can not be used to study the presence of Zn in the S phase, as the weak Zn-L2,3 edge would drown in the stronger signal from the Cu-L2,3 edge. STEM–EDS maps on an aberration-corrected microscope remains more generally applicable, and work will be done to improve the resolution of such maps of precipitates with non-stoichiometric compositions.

Acknowledgements

The authors would like to thank the Research Council of Norway (RCN) for funding of the FRINATEK project "Fundamental investigations of precipitation in the solid state with focus on Al-based alloys". The experimental work was carried out on the NORTEM instrument JEOL JEM-2100F, TEM Gemini Centre, NTNU, Norway. The research was supported by the NOTUR high-performance computing program funded by the RCN.

[1] M. Liu, S. Bai, Z. Liu, X. Zhou, P. Xia, S. Zeng, Mater. Sci. Eng. A 629 (2015) 23–28. doi:10.1016/j.msea.2015.01.079.

[2] M. Mihara, C. D. Marioara, S. J. Andersen, R. Holmestad, E. Kobayashi, T. Sato, Mater. Sci. Eng. A 658 (2016) 91–98. doi:10.1016/j.msea.2016.01.087.

[3] M. Gazizov, R. Kaibyshev, Mater. Sci. Eng. A 625 (2015) 119–130. doi:10.1016/j.msea.2014.11.094.

[4] X. wu Nie, L. jun Zhang, Y. Du, Trans. Nonferr. Metal. Soc. 24 (2014) 2138–2144. doi:10.1016/S1003-6326(14)63324-0.

[5] W. Guo, J. Guo, J. Wang, M. Yang, H. Li, X. Wen, J. Zhang, Mater. Sci. Eng. A 634 (2015) 167–175. doi:10.1016/j.msea.2015.03.047.

[6] Y. Liu, D. M. Jiang, W. J. Li, J. Alloy. Compd. 671 (2016) 408–418. doi:10.1016/j.jallcom.2016.01.266.

[7] J. T. Jiang, Q. J. Tang, L. Yang, K. Zhang, S. J. Yuan, L. Zhen, J. Mater. Process. Tech. 227 (2016) 110–116. doi:10.1016/j.jmatprotec.2015.07.018.

[8] R. Kilaas, V. Radmilovic, Ultramicroscopy 88 (2001) 63–72. doi:10.1016/S0304-3991(00)00107-8.

[9] V. Radmilovic, G. Thomas, G. J. Shiflet, E. A. Starke Jr., Scripta Metall. 23 (1989) 1141–1146.

[10] J. B. Friauf, Phys. Rev. 29 (1927) 34.

[11] Y. Komura, K. Tokunaga, Acta Cryst. B 36 (1980) 1548–1554. doi:10.1107/S0567740880006565.

[12] Y.-Y. Li, L. Kovarik, P. J. Phillips, Y.-F. Hsu, W.-H. Wang, M. J. Mills, Phil. Mag. Lett. 92 (2012) 166–178. doi:10.1080/09500839.2011.652682.

[13] C. D. Marioara, W. Lefebvre, S. J. Andersen, J. Friis, Journal of Materials Science 48 (2013) 3638–3651. doi:10.1007/s10853-013-7158-3.

[14] J. Z. Liu, J. H. Chen, D. W. Yuan, C. L. Wu, J. Zhu, Z. Y. Cheng, Mater Charact. 99 (2015) 277–286.

[15] T. Marlaud, A. Deschamps, F. Bley, W. Lefebvre, B. Baroux, Acta Materialia 58 (2010) 248–260. doi:10.1016/j.actamat.2009.09.003.

[16] S. Wenner, C. D. Marioara, W. Lefebvre, Q. M. Ramasse, D.-M. Kepaptsoglou, F. S. Hage, R. Holmestad, Mater. Sci. Forum 794–796 (2014) 63–67.

[17] Acta Mater. 60 (2012) 3239–3246.

[18] S. C. Wang, M. J. Starink, Int. Mater. Rev. 50 (2005) 193–215.

[19] Z. Q. Feng, Y. Q. Yang, B. Huang, M. H. Li, Y. X. Chen, J. G. Ru, J. Alloy Compd. 583 (2014) 445–451.

[20] G. Kresse, J. Hafner, Phys. Rev. B 47 (1993) 558–561. doi:10.1103/PhysRevB.47.558.

[21] G. Kresse, J. Furthmüller, Phys. Rev. B 54 (1996) 11169–11186.

[22] G. Kresse, D. Joubert, Phys. Rev. B 59 (1999) 1758–1775.

[23] J. P. Perdew, K. Burke, M. Ernzerhof, Phys. Rev. Lett. 77 (1996) 3865–3868.

[24] M. M. A. T. Paxton, Phys. Rev. B 40 (1989) 3616–3621.

[25] Z. R. Liu, J. H. Chen, S. B. Wang, D. W. Yuan, M. J. Yin, C. L. Wu, Acta Mater. 59 (2011) 7396–7405.

[26] L. Kovarik, S. A. Court, H. L. Fraser, M. J. Mills, Acta Mater. 56 (2008) 4804–4815. doi:10.1016/j.actamat.2008.05.042.

[27] C. R. Hutchinson, S. P. Ringer, Metall. Mater. Trans. A 31 (2000) 2721–2733. doi:10.1007/BF02830331.

[28] L. Kovarik, M. K. Miller, S. A. Court, M. J. Mills, Acta Mater. 54 (2006) 1731–1740.